

NONLINEAR TENSOR DIFFUSION IN IMAGE PROCESSING*

OLGA STAŠOVÁ , KAROL MIKULA , ANGELA HANDLOVIČOVÁ†, AND NADINE PEYRIÉRAS‡

Abstract. This paper presents and summarize our results concerning the nonlinear tensor diffusion which enhances image structure coherence. The core of the paper comes from [3, 2, 4, 5]. First we briefly describe the diffusion model and provide its basic properties. Further we build a semi-implicit finite volume scheme for the above mentioned model with the help of a co-volume mesh. This strategy is well-known as diamond-cell method owing to the choice of co-volume as a diamond-shaped polygon, see [1]. We present here 2D as well as 3D case of a numerical scheme, see [3, 4]. Then the convergence and error estimate analysis for 2D scheme is presented, see [3, 2]. Last part is devoted to results of computational experiments. They confirm the usefulness this diffusion type not just for an image improvement but also as a pre-processed algorithm. Numerical techniques which require a good coherence of image structures (like edge detection and segmentation) achieve much better results when we use images pre-processed by such a filtration. Let us note that this diffusion technique was successfully applied within the framework of EU projects. It was used to pre-process images for the structure segmentation in zebrafish embryogenesis, see [5].

Key words. image processing, nonlinear tensor diffusion, coherence enhancing diffusion, numerical solution, semi-implicit scheme, diamond-cell finite volume method, convergence, error estimate, structure segmentation.

AMS subject classifications. 35K55, 65M12, 35B45, 68U10, 65M08.

1. Introduction. Coherence enhancing diffusion (CED), see [11], is a technique which enables to achieve an improvement of image structure connectivity. It is also helpful as a pre-processed algorithm for numerical methods in which a precise image structure coherence is desirable (e.g. edge detection, segmentation). Applying these procedures on images filtered by CED yields an enhancement of their results. The filtration process is driven by the diffusion tensor in such a way that the diffusion is strong in preferred directions, e.g. along edges (in 2D images) or along 2D edge surfaces (in 3D images) which causes a recovery of defects in image structures. Interrupted places will be completed. On the contrary, the smoothing is low in the perpendicular direction and therefore the edges are not significantly blurred.

2. Mathematical model. Let Q_T is a spatio-temporal domain, where a time interval is given by $I = [0, T]$ and Ω (subset of \mathbb{R}^2 or \mathbb{R}^3) is an image domain with the boundary $\partial\Omega$. We consider the coherence enhancing diffusion model on this domain. It has the following form, see [11, 3, 7, 4],

$$(2.1) \quad \frac{\partial u}{\partial t} - \nabla \cdot (D\nabla u) = 0 \quad \text{in } Q_T \equiv I \times \Omega,$$

$$(2.2) \quad u(x, 0) = u_0(x) \quad \text{in } \Omega,$$

$$(2.3) \quad D\nabla u \cdot \mathbf{n} = 0 \quad \text{on } I \times \partial\Omega,$$

*This work was supported by Grants APVV-15-0522 and VEGA 1/0608/15.

†Faculty of Civil Engineering, Slovak University of Technology, Radlinského 11, 810 05 Bratislava, Slovakia (olga.stasova@stuba.sk, karol.mikula@stuba.sk, angela.handlovicova@stuba.sk).

‡Institut de Neurobiologie Alfred Fessard, CNRS-NED, Avenue de la Terrasse, 911 98 Gif-sur-Yvette, France nadine.peyrieras@inaf.cnrs-gif.fr.

where $u(x, t)$ denotes an unknown function and represents a grey level image intensity, $u_0 \in L^2(\Omega)$ and \mathbf{n} denotes the outer normal unit vector to the $\partial\Omega$. The matrix D represents the so-called diffusion tensor. Its design differs in dependence on a dimension order.

2.1. 2D diffusion tensor. The construction of the 2D diffusion tensor is based on the eigenvalues and eigenvectors of the (regularized) structure tensor $J_\rho(\nabla u_{\tilde{t}}) = G_\rho * (\nabla u_{\tilde{t}} \nabla u_{\tilde{t}}^T) = \begin{pmatrix} a & b \\ b & c \end{pmatrix}$, where $u_{\tilde{t}}(x, t) = (G_{\tilde{t}} * u(\cdot, t))(x)$. $G_{\tilde{t}}$ and G_ρ are Gaussian convolution kernels, see [11, 3]. The matrix J_ρ is symmetric and positive semidefinite and its eigenvectors are parallel and orthogonal to $\nabla u_{\tilde{t}}$, respectively. Its eigenvalues are given by $\mu_{1,2} = \frac{1}{2} \left(a + c \pm \sqrt{(a-c)^2 + 4b^2} \right)$, $\mu_1 \geq \mu_2$. The corresponding orthogonal set of eigenvectors (\mathbf{v}, \mathbf{w}) to eigenvalues (μ_1, μ_2) is given as follows

$$(2.4) \quad \begin{aligned} \mathbf{v} &= (v_1, v_2), & \mathbf{w} &= (w_1, w_2), & \mathbf{w} &\perp \mathbf{v}, & w_1 &= -v_2, & w_2 &= v_1, \\ v_1 &= 2b, & v_2 &= c - a + \sqrt{(a-c)^2 + 4b^2}. \end{aligned}$$

The orientation of the eigenvector \mathbf{w} corresponding to the smaller eigenvalue μ_2 is called the coherence orientation. This orientation has the lowest fluctuations in image intensity. The diffusion tensor D is built to steer a filtering process such that the smoothing is strong along the coherence direction \mathbf{w} and increases with the coherence $(\mu_1 - \mu_2)^2$. To achieve it, we require D to possess the same eigenvectors \mathbf{v} and \mathbf{w} as the structure tensor $J_\rho(\nabla u_{\tilde{t}})$ and we choose the eigenvalues of D as follows

$$(2.5) \quad \begin{aligned} \kappa_1 &= \alpha, & \alpha &\in (0, 1), \alpha \ll 1, \\ \kappa_2 &= \begin{cases} \alpha, & \text{if } \mu_1 = \mu_2, \\ \alpha + (1 - \alpha) \exp\left(\frac{-C}{(\mu_1 - \mu_2)^2}\right), & C > 0 \text{ else.} \end{cases} \end{aligned}$$

Hence we get the diffusion tensor in the form

$$(2.6) \quad D = ABA^{-1}, \quad \text{where } A = \begin{pmatrix} v_1 & -v_2 \\ v_2 & v_1 \end{pmatrix} \quad \text{and } B = \begin{pmatrix} \kappa_1 & 0 \\ 0 & \kappa_2 \end{pmatrix},$$

which depends nonlinearly on partial derivatives of solution u , possesses smoothness, symmetry and uniform positive definiteness properties.

2.2. 3D diffusion tensor. The construction of the 3D diffusion tensor is based on a smoothed intensity gradient given by $\nabla u_{\tilde{t}} = (u_{x_1}, u_{x_2}, u_{x_3})^T$, where $u_{\tilde{t}}(x, t) = (G_{\tilde{t}} * u(\cdot, t))(x)$, ($\tilde{t} > 0$) and $G_{\tilde{t}}$ is a Gaussian kernel, see [4, 7]. Provided that $\mu = \|\nabla u_{\tilde{t}}\|^2 > 0$ we choose a triplet of vectors $(\mathbf{v}_1, \mathbf{v}_2, \mathbf{v}_3)$ by $\mathbf{v}_1 \parallel \nabla u_{\tilde{t}}$, $\mathbf{v}_2 \perp \nabla u_{\tilde{t}}$, $\mathbf{v}_3 \perp \nabla u_{\tilde{t}}$, $\mathbf{v}_2 \perp \mathbf{v}_3$. The direction of vector \mathbf{v}_1 corresponds to the direction of the largest intensity change. The other two vectors give a tangential plane to a level set of image intensity which may represent a 2D surface edge in a 3D image, provided that μ is large. It is called coherence plane \mathcal{P} and represents an eigenspace corresponding to the eigenvalue 0 of the outer product $\nabla u_{\tilde{t}} \otimes \nabla u_{\tilde{t}}$. In order to enhance the coherence, the diffusion tensor D must steer the filtering process such that the diffusion is strong and increasing with the level of μ along the coherence plane \mathcal{P} and is small in the perpendicular direction. We achieve it by choosing the eigenvalues of the diffusion tensor, which determine the diffusivities in the directions \mathbf{v}_1 , \mathbf{v}_2 and \mathbf{v}_3 as

$$(2.7) \quad \kappa_1 = \alpha, \quad \alpha \in (0, 1), \alpha \ll 1,$$

$$\kappa_2 = \kappa_3 = \begin{cases} \alpha, & \text{if } \mu = 0, \\ \alpha + (1 - \alpha) \exp\left(\frac{-C}{\mu}\right), & C > 0 \text{ otherwise.} \end{cases}$$

Then we apply another convolution with a smoothing kernel G_ρ and get the diffusion matrix D in the form

$$(2.8) \quad D = G_\rho * D_0, \text{ where } D_0 = \begin{cases} B, & \text{if } \mu = 0, \\ PBB^{-1} & \text{otherwise,} \end{cases} \quad B = \begin{pmatrix} \kappa_1 & 0 & 0 \\ 0 & \kappa_2 & 0 \\ 0 & 0 & \kappa_2 \end{pmatrix}$$

and P denotes a transition matrix from the basis $(\mathbf{v}_1, \mathbf{v}_2, \mathbf{v}_3)$ to $(\mathbf{e}_1, \mathbf{e}_2, \mathbf{e}_3)$. If $\mu > 0$, the matrix D_0 has the following form

$$\frac{1}{\mu} \begin{pmatrix} u_{x_1}^2 \kappa_1 + (u_{x_2}^2 + u_{x_3}^2) \kappa_2 & u_{x_1} u_{x_2} (\kappa_1 - \kappa_2) & u_{x_1} u_{x_3} (\kappa_1 - \kappa_2) \\ u_{x_1} u_{x_2} (\kappa_1 - \kappa_2) & u_{x_2}^2 \kappa_1 + (u_{x_1}^2 + u_{x_3}^2) \kappa_2 & u_{x_2} u_{x_3} (\kappa_1 - \kappa_2) \\ u_{x_1} u_{x_3} (\kappa_1 - \kappa_2) & u_{x_2} u_{x_3} (\kappa_1 - \kappa_2) & u_{x_3}^2 \kappa_1 + (u_{x_1}^2 + u_{x_2}^2) \kappa_2 \end{pmatrix}$$

in the standard basis $(\mathbf{e}_1, \mathbf{e}_2, \mathbf{e}_3)$. Such choice of the matrix D_0 was given in [4], it is independent on a concrete choice of \mathbf{v}_2 and \mathbf{v}_3 and can be directly and fast evaluated using the diamond-cell finite volume technique (see also next section). The 3D diffusion tensor satisfies the smoothness, symmetry and positive definiteness properties, see [4], as does the 2D diffusion tensor.

3. Diamond-cell finite volume scheme. We design the numerical scheme for CED using the finite volume method, see [6], since this discretization technique uses the piecewise constant representation of approximate solutions similarly to the structure of digital images. The restrictions of the classical five-point method for the tensor models, see [8], lead to choice of the nine-point diamond-cell method in 2D, see [1, 3]. Similarly, we switch to 27-point scheme instead of simpler 7-point scheme in 3D space, see [4].

Let the image be represented by $n_1 \times n_2$ pixels (finite volumes) in 2D or by $n_1 \times n_2 \times n_3$ voxels in 3D such that it looks like a mesh with n_1 rows and n_2 columns in 2D or a mesh with n_1 rows, n_2 columns and n_3 layers in 3D. Let $\Omega = (0, n_1 h) \times (0, n_2 h)$ in 2D or $\Omega = (0, n_1 h) \times (0, n_2 h) \times (0, n_3 h)$ in 3D with a pixel(voxel) size h . We consider the filtering process in a time interval $I = [0, T]$. Let the time discretization be given by $0 = t_0 \leq t_1 \leq \dots \leq t_{N_{max}} = T$ with $t_n = t_{n-1} + k$, where k is the length of the discrete time step. \mathcal{T}_h is an admissible finite volume mesh, see [6] and further quantities and notations are given as follows: $m(W)$ is the measure of the finite volume W with boundary ∂W , $\sigma_{WE} = W \cap E = W|E$ is an edge(face) of the finite volume W , where $E \in \mathcal{T}_h$ is an adjacent finite volume to W such that the measure $m(W \cap E) \neq 0$. At several places we will replace σ_{WE} by σ to simplify notation. $m(\sigma)$ is the measure of edge (face) σ . \mathcal{E}_W represents the set of edges(faces) such that $\partial W = \bigcup_{\sigma \in \mathcal{E}_W} \sigma$ and $\mathcal{E} = \bigcup_{W \in \mathcal{T}_h} \mathcal{E}_W$. The set of boundary edges(faces) is denoted by \mathcal{E}_{ext} , that is $\mathcal{E}_{ext} = \{\sigma \in \mathcal{E}, \sigma \subset \partial\Omega\}$ and denote $\mathcal{E}_{int} = \mathcal{E} \setminus \mathcal{E}_{ext}$. Υ is the set of pairs of adjacent finite volumes, defined by $\Upsilon = \{(W, E) \in \mathcal{T}_h^2, W \neq E, m(\sigma_{WE}) \neq 0\}$ and $\mathbf{n}_{W,\sigma}$ is the normal unit vector to σ outward to W . Let u_W^n represents a numerical solution on finite volume W , $W \in \mathcal{T}_h$ at time t_n , $n = 1, \dots, N_{max}$.

Our discrete solution is given by $u_{h,k}(x, t) = \sum_{n=0}^{N_{max}} \sum_{W \in \mathcal{T}_h} u_W^n \chi_{\{x \in W\}} \chi_{\{t_{n-1} < t \leq t_n\}}$ where the function $\chi_{\{A\}}$ is defined as

$$\chi_{\{A\}} = \begin{cases} 1, & \text{if } A \text{ is true,} \\ 0, & \text{elsewhere.} \end{cases}$$

The finite volume approximation at the n -th time step is given by

$$u_{h,k}^n(x) = \sum_{W \in \mathcal{T}_h} u_W^n \chi\{x \in W\}$$

and initial values as $u_W^0 = \frac{1}{m(W)} \int_W u_0(x) dx$, $W \in \mathcal{T}_h$.

We start the scheme derivation integrating the equation (2.1) over the finite volume W , then provide a semi-implicit discretization and use the divergence theorem to have

$$(3.1) \quad \frac{u_W^n - u_W^{n-1}}{k} m(W) - \sum_{\sigma \in \mathcal{E}_W \cap \mathcal{E}_{int}} \int_{\sigma} (D^{n-1} \nabla u^n) \cdot \mathbf{n}_{W,\sigma} ds = 0.$$

We can define an auxiliary unknown $\phi_{\sigma}^n(u_{h,k}^n)$ representing an approximation of the exact averaged flux $\frac{1}{m(\sigma)} \int_{\sigma} (D^{n-1} \nabla u^n) \cdot \mathbf{n}_{W,\sigma} ds$ for any W and $\sigma \in \mathcal{E}_W$ in order to rewrite (3.1) in the form

$$(3.2) \quad \frac{u_W^n - u_W^{n-1}}{k} - \frac{1}{m(W)} \sum_{\sigma \in \mathcal{E}_W \cap \mathcal{E}_{int}} \phi_{\sigma}^n(u_{h,k}^n) m(\sigma) = 0.$$

Approximation of the flux $\phi_{\sigma}^n(u_{h,k}^n)$ is built with the help of a co-volume mesh, see e.g. [1, 3]. The $2D$ co-volume χ_{σ} associated to σ is constructed around each edge by joining endpoints of this edge and midpoints of finite volumes which are common to this edge, see Fig. 3.1. We create a co-volume χ_{σ} associated with σ around each

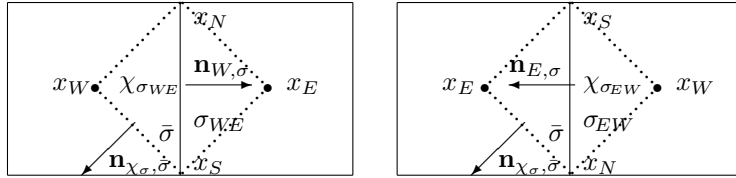


FIG. 3.1. The co-volumes χ_{σ} associated to edges $\sigma = \sigma_{WE}$ (left) and $\sigma = \sigma_{EW}$ (right).

finite volume face by joining four vertices of this face and midpoints of the finite volumes which are common to this face, see Fig. 3.2. Using this technique we obtain the scheme in the form, see [3, 4],

$$(3.3) \quad \frac{u_W^n - u_W^{n-1}}{k} - \frac{1}{m(W)} \sum_{\sigma \in \mathcal{E}_W \cap \mathcal{E}_{int}} \phi_{\sigma}^n(u_{h,k}^n) m(\sigma) = 0$$

$$(3.4) \quad \text{with } 2D \phi_{\sigma}^n(u_{h,k}^n) = \bar{D}_{11}^{\sigma} \frac{u_E^n - u_W^n}{h} + \bar{D}_{12}^{\sigma} \frac{u_N^n - u_S^n}{h},$$

$$(3.5) \quad \text{with } 3D \phi_{\sigma}^n(u_{h,k}^n) = \bar{D}_{11}^{\sigma} \frac{u_E^n - u_W^n}{h} + \bar{D}_{12}^{\sigma} \frac{u_{TN}^n + u_{BN}^n - u_{TS}^n - u_{BS}^n}{2h} + \bar{D}_{13}^{\sigma} \frac{u_{TN}^n + u_{TS}^n - u_{BN}^n - u_{BS}^n}{2h}.$$

where \bar{D}_{11}^{σ} and \bar{D}_{12}^{σ} in $2D$ $\phi_{\sigma}^n(u_{h,k}^n)$ are elements of the matrix $D_{\sigma} = D_{\sigma}^{n-1}$ written in the basis $(\mathbf{n}_{W,\sigma}, \mathbf{t}_{W,\sigma})$, see [1], where $\mathbf{t}_{W,\sigma}$ is a unit vector parallel to σ such that $(x_N - x_S) \cdot \mathbf{t}_{W,\sigma} > 0$. The values at x_E and x_W are taken as u_E and u_W , and the

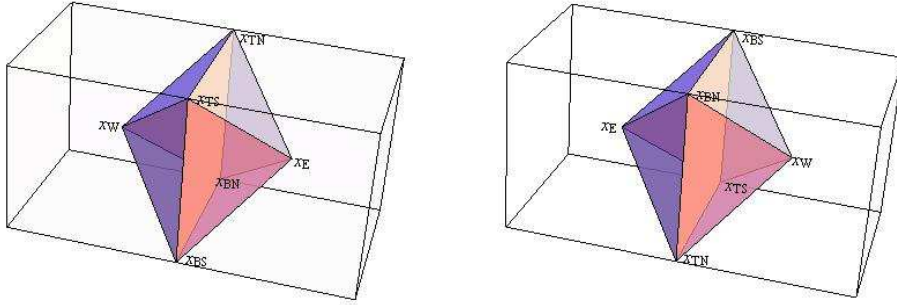


FIG. 3.2. The co-volumes associated with the face $\sigma = \sigma_{WE}$ (left) and $\sigma = \sigma_{EW}$ (right).

values u_S and u_N at the vertices x_N and x_S are computed as the arithmetic mean of u_W , where W are finite volumes which are common to this vertex. Further, \bar{D}_{11}^σ , \bar{D}_{12}^σ and \bar{D}_{13}^σ in $3D \phi_\sigma^n(u_{h,k}^n)$ are elements of the matrix $D_\sigma = D_\sigma^{n-1}$ written in the basis $(\mathbf{n}_{W,\sigma}, \mathbf{t}_{1W,\sigma}, \mathbf{t}_{2W,\sigma})$, where $\mathbf{t}_{1K,\sigma}$ is a unit vector parallel to $x_{TN} - x_{TS}$ such that $(x_{TN} - x_{TS}) \cdot \mathbf{t}_{1K,\sigma} > 0$ and $\mathbf{t}_{2K,\sigma}$ is a unit vector parallel to $x_{TN} - x_{BN}$ such that $(x_{TN} - x_{BN}) \cdot \mathbf{t}_{2K,\sigma} > 0$. Due to the computation of the values u_{TN} , u_{TS} , u_{BN} and u_{BS} in (3.5) as the arithmetic mean of neighbouring voxel values, we get the 27 point finite volume scheme.

4. Convergence analysis for 2D discrete scheme. We proved the convergence of the numerical solution of the scheme (3.3)-(3.4) to the weak solution of the problem (2.1)-(2.3) in [3]. Our convergence analysis follows the convergence proof from [8], see [3]. However, our scheme is 9-point scheme compared with the 5-point scheme from [8]. Due to this fact, we must take into account also values of corner's neighbouring volumes. They appear in the scheme in the form of a derivative in the tangential direction, since u_N and u_S are computed as arithmetical mean of their 4 adjacent volumes. In order to overcome the difficulties arising in the occurrence of u_N and u_S we bound the derivative in tangential direction by using the derivative in normal direction with the help of the following lemma.

LEMMA 4.1. (Bounding of the derivative in tangential direction) *The derivative in tangential direction is bounded by the derivative in normal direction (see Fig. 3.1) as follows*

$$(4.1) \quad \sum_{\sigma \in \mathcal{E}_{int}} \left(\frac{\bar{D}_{12}^\sigma}{\bar{D}_{11}^\sigma} \right)^2 \left(\frac{u_N^n - u_S^n}{h} \right)^2 \bar{D}_{11}^\sigma \leq \gamma \sum_{\sigma \in \mathcal{E}_{int}} \left(\frac{u_E^n - u_W^n}{h} \right)^2 \bar{D}_{11}^\sigma,$$

where $0 \leq \gamma < 1$, $\gamma = \max_{\sigma \in \mathcal{E}} \gamma_\sigma$, $\gamma_\sigma = \sum_{\delta \in P_\sigma \cap \mathcal{E}_{int}} \frac{1}{4} \left(\frac{\bar{D}_{12}^\delta}{\bar{D}_{11}^\delta} \right)^2 \frac{\bar{D}_{11}^\delta}{\bar{D}_{11}^\delta}$,

where edges δ and set P_σ are given in the following definition.

DEFINITION 4.2. Let P_σ be the set of all edges δ perpendicular to σ , which have common vertex with σ and fulfill the following conditions:

$(x_{E_\delta} - x_{W_\delta}) \cdot \mathbf{t}_{W,\sigma} > 0$ if $(x_{N_\sigma} - x_{S_\sigma}) \cdot \mathbf{t}_{W,\sigma} > 0$ and
 $(x_{E_\delta} - x_{W_\delta}) \cdot \mathbf{t}_{W,\sigma} < 0$ if $(x_{N_\sigma} - x_{S_\sigma}) \cdot \mathbf{t}_{W,\sigma} < 0$,
 which means that $x_{E_\delta} - x_{W_\delta}$ has the same orientation as the tangent $\mathbf{t}_{W,\sigma}$. Let us note that $x_{W_\sigma} = x_{W_\delta}^1 = x_{E_\delta}^3$, for $\sigma = \sigma_{WE}$, $x_{E_\sigma} = x_{W_\delta}^2 = x_{E_\delta}^4$, for $\sigma = \sigma_{WE}$, $x_{W_\sigma} = x_{E_\delta}^2 = x_{W_\delta}^4$, for $\sigma = \sigma_{EW}$ and $x_{E_\sigma} = x_{E_\delta}^1 = x_{W_\delta}^3$, for $\sigma = \sigma_{EW}$.

Our convergence proof is based on Kolmogorov's compactness theorem. We proved the following lemmata: Uniform boundedness, Time translate estimate, Space translate estimate and stronger Space translate estimate in [3]. Using these lemmata we know that the sequence of discrete solution $u_{h,k}$ is relatively compact in L^2 , which implies that there exists a subsequence of $u_{h,k}$ which is bounded. The main theorem of the convergence analysis is given below.

THEOREM 4.3. (Convergence of the scheme) *The sequence $u_{h,k}$ converges strongly in $L^2(Q_T)$ to the unique weak solution u of (2.1)-(2.3) as $h, k \rightarrow 0$.*

The crucial ideas used in our convergence proof are the convergence of the discrete weak form to the continuous weak form, which follows from the Lipschitz continuity of diffusion tensor elements and the fact that the limit u of $u_{h,k}$ is in space $L^2(0, T; H^1(\Omega))$, which follows from stronger Space translate estimate. The detailed convergence proof can be found in [3].

5. Error estimate analysis. This section concerns with an estimate of the difference between the weak solution of the model (2.1)-(2.3) and the numerical solution satisfying the scheme (3.3)-(3.4) in dependence on spatial and time discretization step, see [2]. Subtracting the discrete form from the continuous form and rearranging it we get a relation. It can be split in several terms and each of them can be bounded. Using these estimations we can state the following theorem.

THEOREM 5.1. (Error estimate) *Let the weak solution fulfil the following regularity properties: $\nabla u \in L_\infty(Q_T)$, $u_{tt} \in L_2(Q_T)$, $u \in L_2(I, W^{2,2}(\Omega))$, $\nabla u_t \in L_2(I, L_\infty(\Omega))$. Let $e_W^n = u(x_W, t_n) - u_W^n$ and $e_{h,k}^n(x, t) = \sum_{W \in \mathcal{T}_h} e_W^n \chi_{\{x \in W\}} \chi_{\{t_{n-1} < t \leq t_n\}}$. Then, there exist a constant C , such that for sufficiently small h*

$$\int_{\Omega} |e_{h,k}^m|^2 dx + \sum_{n=1}^m \int_{\Omega} |e_{h,k}^n - e_{h,k}^{n-1}|^2 dx + \sum_{n=1}^m \int_{t_{n-1}}^{t_n} \sum_{\sigma \in \mathcal{E}_{int}} (e_E^n - e_W^n)^2 dt \leq C(h^2 + k)$$

for every $m = 1, \dots, N_{\max}$.

One can observe that the error of the piecewise constant approximation given by our scheme in $L_\infty(I, L_2)$ is of order h . The core of error estimate proof consists of a bounding of the derivative in tangential direction by means of the derivative in normal direction, a time translate estimate for approximate solution and the Lipschitz continuity of the diffusion tensor elements with respect to the smoothed partial derivatives of the solution. The detailed error estimate proof is given in [2].

Let us note that the 3D convergence / error estimate analysis is still an outstanding problem since we are not yet able to extend the inequality from Lemma 4.1 to its 3D version.

6. Computational experiments. The goal of this section is to demonstrate benefits of our numerical technique. We performed our experiments on a 2D fingerprint image (type of flow-like structures image) and 3D image sequences coming from the two-photon laser scanning microscopy. They represent early stages of zebrafish embryogenesis.

First experiment represents the behaviour of the CED (coherence enhancing diffusion). This technique yields a coherence improvement of image flow-like structures. After several filtration steps round interrupted places become gradually elongated in the coherence direction and they will be eventually corrected, see Fig. 6.1 and Fig. 6.2. We used the following filtration parameters: a space step 0,01, a time step 0,0001,

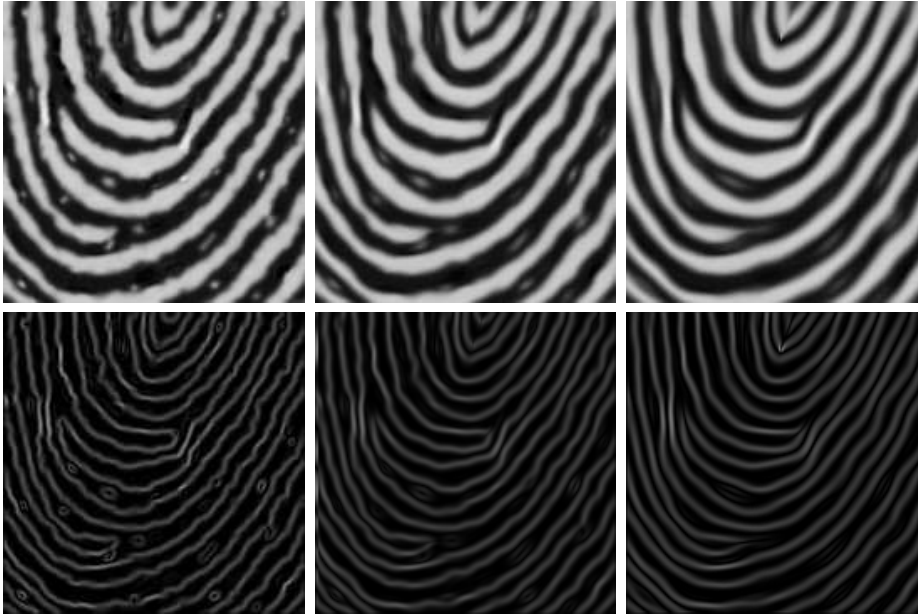


FIG. 6.1. A fingerprint image. Top: the original image(left), the filtered image after 5 time steps(middle) and the filtered image after 20 time steps(right). Bottom: the Sobel edge detections of these images.

$\tilde{t} = 0,000025$ and $\rho = 0,002$. Fig. 6.1 shows a fingerprint image. The original image is deteriorated by numerous redundant apertures while most of them are lost in the filtered image. Fig. 6.2 depicts damaged cell membranes. Some boundaries are almost lost in the original image, but we are able to clearly recognize them in the filtered image.

6.1. Pre-processing technique. Further, we concern our method as a pre-processing technique. We show its contribution to the subsequent image algorithms. If we pre-process images for techniques which depend on the connectivity of coherent image structures by the CED, we achieve significantly better results. We can adduce an edge detection as an example. If we compare the edge detections of an original and filtered image, see Fig. 6.1 and Fig. 6.2 (bottom), we can observe that the edge detection of the original image depicts many superfluous image structures caused by noise which are omitted in the edge detection of the filtered image. Moreover, several boundaries which are lost in the first edge detection are reconstructed in the second edge detection, see Fig. 6.2 (bottom).

The structure segmentation, see [5], is also the post-processing algorithm following CED. We use the segmentation based on the subjective surface method, see [10] and its finite volume implementation from [9]. The segmentation model has the following form

$$(6.1) \quad \partial_t u = \sqrt{\varepsilon^2 + |\nabla u|^2} \nabla \cdot \left(g(|\nabla G_\sigma * I^0|) \frac{\nabla u}{\sqrt{\varepsilon^2 + |\nabla u|^2}} \right) \quad \text{in } Q_T \equiv I \times \Omega,$$

$$(6.2) \quad u(x, 0) = u_0(x) \quad \text{in } \Omega,$$

$$(6.3) \quad u = 0 \quad \text{on } I \times \partial\Omega,$$

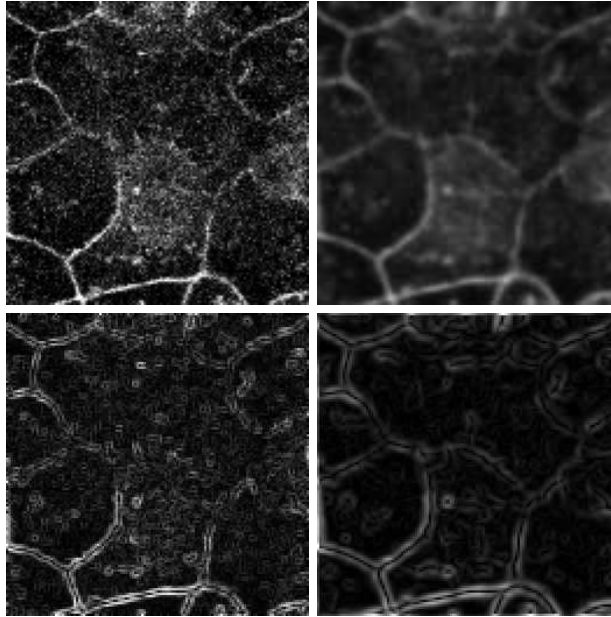


FIG. 6.2. Cell membranes. Top: the original image(left) and the filtered image after 5 time steps(right). Bottom: the Sobel edge detections of these images.

where I^0 is the image intensity and ε is the regularization parameter. The solution u denotes the evolving segmentation function. The function $g = g(|\nabla G_\sigma * I^0|)$ has the role of the edge detector. We start the segmentation imposing the initial segmentation function in an approximate center of segmented object. This function is evolved by equation (6.1) to a final steady state which gives the boundaries of the segmented object. The question is which isoline of the final steady state most precisely represents the object shape. The chosen isoline is most naturally taken as the average of maximal and minimal value of the final segmentation function.

The goal of this experiment is to segment an eye retina of a zebrafish embryo. Let us note that the structure segmentation is much more complicated than image segmentation since evolving segmentation function is restrained to achieve correct segmentation steady state by fine image objects representing inner cell structures. In order to overcome these constraints we pre-processed images for the segmentation by the CED. Even though they look too blurred they are very suitable for the structure segmentation, see Fig. 6.3. The segmentation result for the original image consists of amount of various isolines and chosen medium isoline bounds only a part of segmented object. On the contrary, the final segmentation function for the image filtered by the CED is represented by a variety of almost identical isolines and each of them precisely illustrates shape of segmented object.

In order to compare our method with other filtration techniques, we pre-processed images for segmentation by the GMCF (geodesic mean curvature flow), MCF (mean curvature flow) and PM (Perona-Malik) smoothing. Fig. 6.4 depicts their segmentation results which are much worse than the final steady state achieved by the coherence enhancing technique. It is caused by the fact that this diffusion not only smooths noise and image objects but emphasizes image structure boundaries as well.

Last experiment is devoted to results of the 3D CED as well as the 3D segmen-

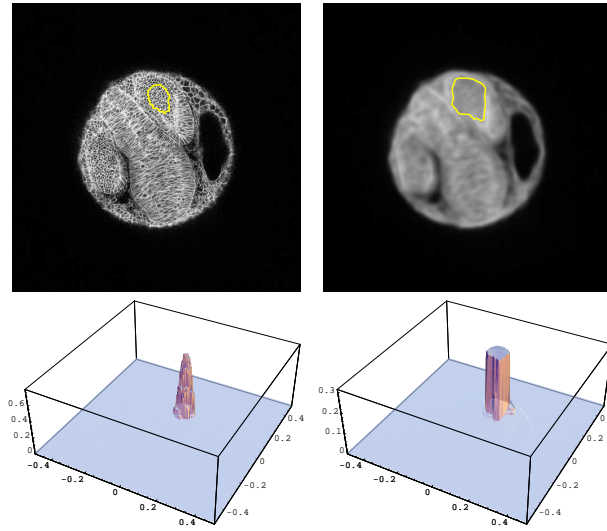


FIG. 6.3. The eye retina segmentation using the 2D slice of 3D original image (left) and the 2D slice of 3D image filtered by 20 time steps of the 3D nonlinear tensor diffusion (right). Top: the averaged isoline of the final state of segmentation function is superimposed to the original and filtered slice, respectively. Bottom: the graph of the final state of segmentation function is plotted after 2000 segmentation time steps using the original slice and after 200 time steps using the filtered slice.

tation algorithms, see Fig. 6.5. These techniques were performed on the 3D image detail representing two cell nuclei. One can observe that the original image is much more deteriorated by a noise than the image filtered by the CED and the noise of the filtered image is less distinct. The contours of the filtered nuclei are smoother than the nucleus contours from the original image since the diffusion tensor of the CED steers the smoothing process in such a way that the diffusion is strong along the coherence plane and very low in the perpendicular direction to this plane. Owing to the above mentioned facts we achieved more precise segmentation results for the nuclei filtered by CED, cf. Fig. 6.5(left) and (right).

The experiments mentioned before confirm the utility of this filtration as a pre-processing technique for algorithms which depend on the connectivity of coherent image structures.

REFERENCES

- [1] Y. COUDIERE, J. P. VILA AND P. VILLEDIEU, *Convergence rate of a finite volume scheme for a two-dimensional convection-diffusion problem*, M2AN Math. Model. Numer. Anal., 33, (1999), pp. 493–516.
- [2] O. DRBLÍKOVÁ, A. HANDLOVIČOVÁ AND K. MIKULA, *Error Estimates of the Finite Volume Scheme for the Nonlinear Tensor Anisotropic Diffusion*, Applied Numerical Mathematics, 59(10) (2009), pp. 2548–2570.
- [3] O. DRBLÍKOVÁ AND K. MIKULA, *Convergence Analysis of Finite Volume Scheme for Nonlinear Tensor Anisotropic Diffusion in Image Processing*, SIAM J. Numer. Anal., 46(1) (2007), pp. 37–60.
- [4] O. DRBLÍKOVÁ AND K. MIKULA, *Semi-implicit Diamond-cell Finite Volume Scheme for 3D Nonlinear Tensor Diffusion in Coherence Enhancing Image Filtering*, Finite Volumes for Complex Applications, Proceedings of the 5th International Symposium on Finite Volumes for Complex Applications (FVCA5). Published in Great Britain and the United States in

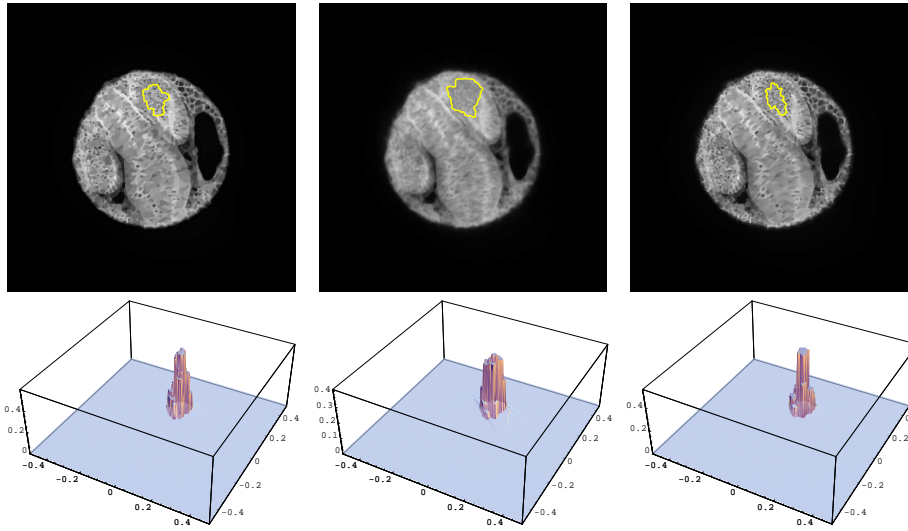


FIG. 6.4. The eye retina segmentation using the 2D slice of the 3D image filtered by 100 steps of the 3D GMCF filtering (left), 25 steps of the 3D MCF filtering (middle) and 20 steps of the 3D PM filtering (right). Top: the averaged isoline of the final state of segmentation function is superimposed to the filtered slice. Bottom: the graph of the final state of segmentation function is plotted after 3000 segmentation steps using the GMCF filtering, after 500 segmentation steps using the MCF filtering and after 5000 segmentation steps using the PM filtering.

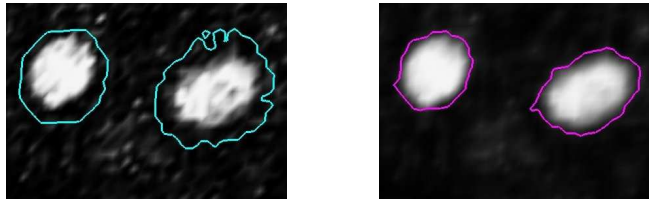


FIG. 6.5. 3D nucleus segmentation using the 3D original image (left) and using the 3D image filtered by 10 time steps (right).

- 2008 by ISTE Ltd and John Wiley & Sons, Inc., ISBN 978-1-84821-035-6, pp. 343–350.
- [5] O. DRBLÍKOVÁ, K. MIKULA AND N. PEYRIÉRAS, *The Nonlinear Tensor Diffusion in Segmentation of Meaningful Biological Structures from Image Sequences of Zebrafish Embryogenesis*, Scale Space and Variational Methods in Computer Vision, Proceedings. Springer Berlin Heidelberg (2009), pp. 63–74.
- [6] R. EYMARD, T. GALLOUËT AND R. HERBIN, *Finite Volume Methods*, in: Handbook for Numerical Analysis, Vol. 7 (Ph. Ciarlet, J. L. Lions, eds.), Elsevier (2000).
- [7] E. MEIJERING, W. NIESSEN, J. WEICKERT, M. VIERGEVER, *Diffusion-Enhanced Visualization and Quantification of Vascular Anomalies in Three-Dimensional Rotational Angiography*, Results of an In-Vitro Evaluation. Medical Image Analysis, 6(3) (2002), pp. 217–235.
- [8] K. MIKULA AND N. RAMAROSY, *Semi-implicit finite volume scheme for solving nonlinear diffusion equations in image processing*, Numer. Math. 89 (3), (2001) pp. 561–590.
- [9] K. MIKULA, A. SARTI, F. SGALLARI, *Co-volume level set method in subjective surface based medical image segmentation*, in: Handbook of Medical Image Analysis: Segmentation and Registration Models (J. Suri et al., Eds.), Springer, New York, (2005) pp. 583–626.
- [10] A. SARTI, R. MALLADI, J.A. SETHIAN, *Subjective Surfaces: A Method for Completing Missing Boundaries*, Proceedings of the National Academy of Sciences of the United States of America, 12 (97), (2000) pp. 6258–6263.
- [11] J. WEICKERT, *Coherence-enhancing diffusion filtering*, Int. J. Comput. Vision, Vol. 31, (1999) pp. 111–127.